Università degli Studi di Napoli "Federico II"

SCUOLA POLITECNICA E DELLE SCIENZE DI BASE

DIPARTIMENTO DI INGEGNERIA INDUSTRIALE

CORSO DI LAUREA IN INGEGNERIA AEROSPAZIALE

CLASSE DELLE LAUREE IN INGEGNERIA INDUSTRIALE (L-9)

Elaborato di laurea in Meccanica del Volo

Geometric modelling, stability and control analysis of an unmanned aerial vehicle with a fixed slot flap

Relatore:
Prof. Danilo Ciliberti

Candidato:
Pepe Miriana
Matr. N35003756

ANNO ACCADEMICO 2024 – 2025

Abstract

This thesis presents the geometric modeling and aerodynamic analysis of an unmanned aerial vehicle (UAV) similar to the Elbit Hemes 900, using the open-source software OpenVSP. OpenVSP is a parametric tool that allows for the creation of a 3D aircraft model, which is subsequently used to perform the stability and control analyses through the VSPAERO tool, a fast and reliable solver based on the Vortex Lattice Method (VLM). This solver provides aerodynamic properties in the early stages of the design process by representing the UAV's lifting surfaces as infinitesimally thin sheets of discrete vortices. While the tool has certain limitations when applied to more complex models, it has proven to be a reasonable and efficient solution for this study, enabling rapid and effective preliminary analysis through careful simulation setup and geometric refinement.

Sommario

Questa tesi presenta la modellazione geometrica e l'analisi aerodinamica di un velivolo senza pilota simile ad un Elbit Hermes 900 (UAV) utilizzando il software open-source OpenVSP. OpenVSP è uno strumento parametrico che consente la creazione di un modello 3D di un aeromobile, successivamente utilizzato per eseguire le analisi di stabilità e controllo tramite lo strumento VSPAERO, un solutore veloce ed affidabile basato sul metodo Vortex Lattice (VLM). Questo solver fornisce le proprietà aerodinamiche durante le prime fasi del processo di progettazione, rappresentando le superfici portanti dell'UAV come lastre infinitamente sottili di vortici discreti. Sebbene lo strumento presenti alcune limitazioni quando è applicato a modelli più complessi, si è dimostrato una soluzione ragionevole ed efficiente per questo studio, consentendo un'analisi preliminare ed affidabile grazie ad un'accurata configurazione della simulazione e una rifinitura del modello geometrico.

Table of contents

List of figures

List of tables

1. Introduction

1.1 Objectives

The aim of this thesis is to provide a comprehensive representation of the aerodynamic and stability analysis of an aircraft similar to the Elbit Hermes 900. The first goal is to model the vehicle and deliver preliminary stability and control data for an aircraft model intended for wind tunnel testing. Additionally, this thesis explains the Vortex Lattice Method (VLM), outlining its fundamental theory, its limitations and its connection to the software used. The study also includes data collection performed with VSPAERO and further processed in Microsoft Excel, to present a detailed overview of the UAV's characteristics. The processed data includes lift, aerodynamic efficiency, moment coefficient, and drag polar curves for the complete aircraft. It is also analyzed the UAV's behavior making the comparison between the single-component wing and the two-components wing.

1.2 Layout of work

Chapter 1: A brief introduction of the aircraft and its major features.

Chapter 2: Vortex Lattice Method and its application in VSPAERO.

Chapter 3: The 3D modelling process in OpenVSP.

Chapter 4: Longitudinal stability and control analysis.

Chapter 5: Lateral-directional stability analysis.

Chapter 6: Conclusions.

1.3 Elbit Hermes 900

The Elbit Hermes 900, also known as ***Kochav*** ("Star"), is an Israeli unmanned aerial vehicle (UAV), developed by Elbit Systems for tactical missions and successor to the Hermes 450, one of the most widely used military drones in the world.

It is a medium-altitude long-endurance (MALE) vehicle, capable of flying for over 30 hours at a maximum altitude of 30,000 feet. This UAV is equipped to carry a payload of 300 kilograms, including advanced electro-optical sensors, synthetic-aperture radar/ground moving target indication and hyperspectral sensors and its ability to carry various payloads makes it suitable for a wide range of missions, including intelligence gathering, border patrol and disaster management.

The Hermes 900 was originally designed for a variety of missions, including reconnaissance, surveillance and communications relays, and it was first used during the 2014 Israel's war in Gaza, even though it was still undergoing test flights and wasn't planned for operational deployment until late 2015. After further integration and flight testing, the Hermes 900 met all the necessary milestones and was officially introduced into the Israeli Air Force's operational lineup in 2015.

Figure 1.1 *The Elbit Hermes 900*

Built with a combination of metal, light alloys, and composite materials, the Hermes 900 features a straight-wing monoplane design with retractable tricycle landing gear and a distinctive V-tail as shown in Figure 1.1. Powered by a four-cylinder, turbocharged Rotax Type 914 engine, it operates with such efficiency that it remains almost imperceptible from the ground when cruising at altitude.

The success of the Hermes 900 extends beyond Israel. This drone has been sold for military use to several countries, including Brazil, India, Azerbaijan, Canada, Chile, Colombia and even the European Union which uses these drones for operations of the European Maritime Safety Agency.

1.3.1 UAV flight stability and control

Stability refers to the UAV's tendency to return to a condition of equilibrium after being subjected to disturbance. It is classified into two main types:

- Static stability: the aircraft's initial response to a disturbance in its attempt to return to equilibrium.
- Dynamic stability: the aircraft's behavior over time following the disturbance.

Stability can also be positive, negative or neutral:

- Neutral stability occurs when the aircraft continues to oscillate without experiencing any decrease or increase in the magnitude of the oscillations.
- Positive stability occurs when the oscillations gradually decrease in magnitude over time.
- Negative stability occurs when the oscillations increase over time.

Neutral stability is achieved when the center of gravity (CG) is located at the neutral point (NP). If the CG is ahead of the NP, the aircraft will exhibit static stability. On the contrary, if the CG is behind the NP, it leads to static instability.

The condition for positive static longitudinal stability is expressed in terms of the Static Margin (SM), which is defined as the difference between the NP and the CG, divided by the mean aerodynamic cord (MAC). Since static stability depends on the CG's position, as previously said, to have positive static longitudinal stability, the SM must be positive.

A large SM implies a very stable but not particularly maneuverable aircraft, whereas a low but positive SM allows the UAV to be highly maneuverable.

During flight, moments on a UAV are created by the aerodynamic load distribution and the thrust force not acting through the CG. Aerodynamic moments are expressed in terms of the dimensionless coefficients for pitching moment (C_m), rolling moment (C_l) and yawing moment (C_n). These values depend on the angle of attack (α), Reynolds (Re), Mach number (M) and sideslip angle (β). An insight into the stability conditions is shown in Figure 1.2.

A necessary condition for longitudinal static stability of the UAV is that the pitching moment curve has a negative slope through the equilibrium point. Also, to trim the vehicle at a positive angle of attack and produce useful lift, the C_m at $\alpha = 0°$ must be greater than zero. The slope must be negative for lateral static stability and positive for directional static stability [1].

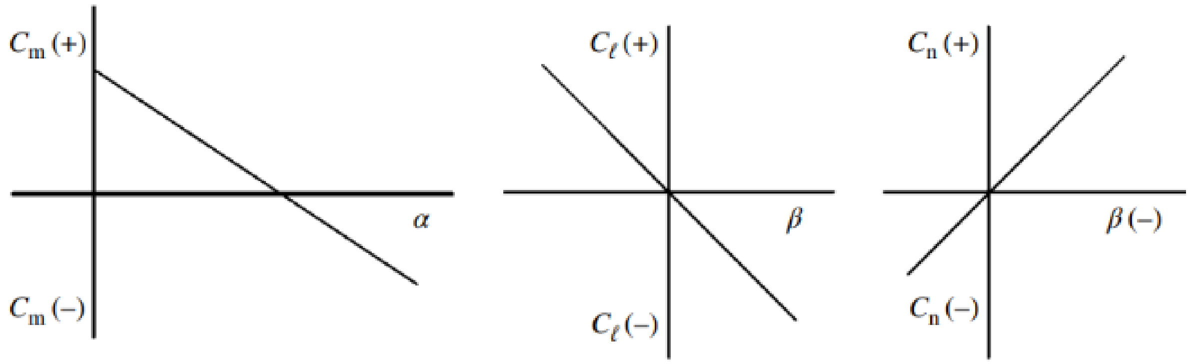

Figure 1.2 *Stability conditions in pitch, roll and yaw*

2. Vortex Lattice Method

The Vortex Lattice Method (VLM) is a numerical method used in computational fluid dynamics, particularly in the early stages of aircraft design, for analyzing the aerodynamic characteristics of lifting surfaces. The VLM models the lifting surfaces, such as wings, as an infinitely thin sheet of discrete vortices and can compute the velocity flow around the wing with relatively low computational cost. By simulating the flow field, this method allows for the extraction of pressure distribution and induced drag, values that are essential to compute aerodynamic coefficients and their derivatives and to optimize aerodynamic performance.

2.1 Theoretical background

2.1.1 Assumptions

This method is built on the theory of ideal flow, also known as potential flow. It is also based on the following assumptions:

1. The flow is incompressible, inviscid and irrotational.
2. The lifting surfaces are thin therefore the influence of the thickness on aerodynamic forces is neglected.
3. The angle of attack and the angle of sideslip are assumed to be small.

2.1.2 Flow description

Since the flow is assumed to be irrotational, vorticity is zero at every point:

$$\xi = \nabla \times \mathrm{V} = 0 \tag{2.1}$$

This implies that the velocity field has no rotational components and can be described by a scalar function φ, such that:

$$\nabla \times (\nabla\varphi) = 0 \tag{2.2}$$

Combining (2.1) and (2.2) we get:

$$\mathrm{V} = \nabla\varphi \tag{2.3}$$

This formula asserts that, for an irrotational flow, it exists a scalar function φ, such that the velocity field is described by its gradient. Hence, we will consider φ as the velocity potential.

From the mass conservation principle for incompressible flow:

$$\nabla \cdot V = 0 \tag{2.4}$$

Using the definition of the velocity potential and integrating (2.3) and (2.4) we obtain:

$$\nabla \cdot (\nabla\varphi) = 0 \tag{2.5}$$

Or equivalently,

$$\nabla^2\varphi = 0 \tag{2.6}$$

This is also known as the Laplace equation, which governs irrotational and incompressible flow. Although the VLM doesn't solve directly the Laplace equation, the vortices it uses are a representation of flows that satisfy the same conditions upon which this equation is based. As a result, a complex model flow, such as the one for an irrotational and incompressible flow, can be synthesized by summing a series of elementary flows that are also irrotational and incompressible.

2.1.3 Boundary conditions

The Vortex Lattice Method (VLM) employs the thin airfoil boundary conditions, which consist in linearizing pressure coefficients and neglecting the effect of thickness and viscosity as shown in Figure 2.1. Additionally, the camber effect on symmetrical airfoils can also be neglected therefore, after applying these boundary conditions to the Laplace equation, the problem can be solved by considering the effect of the angle of attack α on a flat surface.

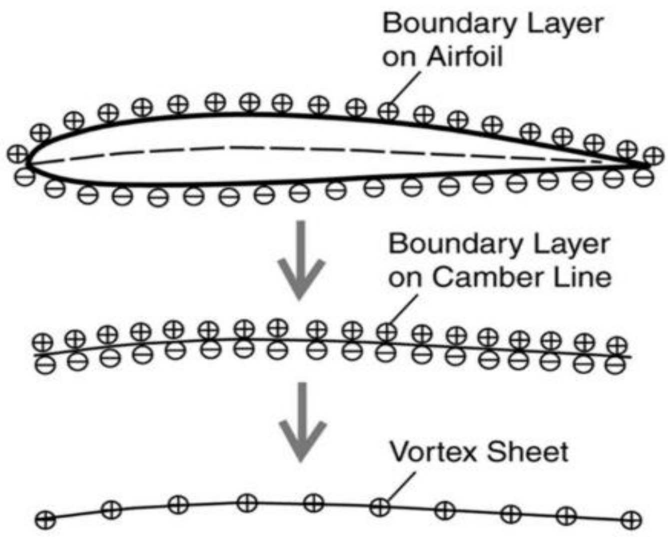

Figure 2.1 Idealization process from a boundary layer to a vortex sheet.

The stated boundary conditions also enforce the principle that the normal flow across the wing's solid surface must be zero and that means that the sum of the component of the velocity normal to the wing must be zero. The total velocity is the sum of:

- The free stream velocity V_∞
- The velocity induced by the wing's bound vortices w_b
- The velocity induced by the wake vortices w_i.

2.1.4 Biot-Savart and horseshoe vortex

One possible solution to the Laplace equation is the singularity of the point vortex, which can be generalized in a three-dimensional filament of a vortex. The mathematical model that describes the flow induced by this filament is the Biot-Savart law (Figure 2.2). It states that the induced velocity dV_p at a point *P*, due to a segment *dl* of a vortex filament dl at a point *q* is:

$$dV_p = \frac{\Gamma}{4\pi} \cdot \frac{dl \times r_{pq}}{|r_{pq}|^3} \tag{2.7}$$

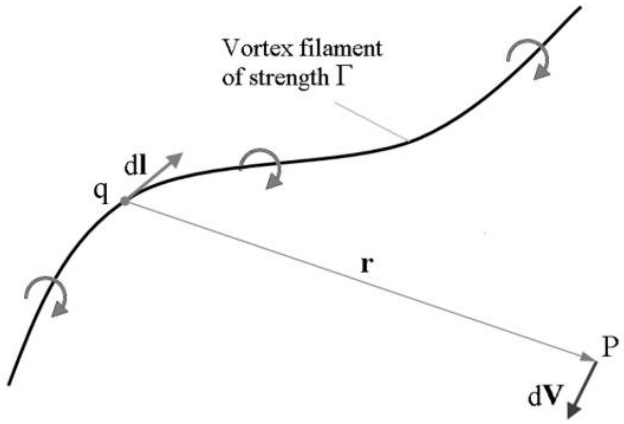

Figure 2.2 Velocity induced by a vortex filament

Integrating along the length of the vortex filament allows to obtain the total velocity induced at a point P:

$$V_p = \frac{\Gamma}{4\pi} \cdot \int \frac{dl \times r_{pq}}{|r_{pq}|^3} \tag{2.8}$$

The VLM employs a specific type of vortex, called the horseshoe vortex. More specifically, the VLM is an extension of Prandtl's lifting-line theory, where the aircraft wing is modeled as an infinite number of horseshoe vortices. In the VLM the wing's surface is divided into a finite number of panels. Each panel has its own horseshoe vortex, and each vortex has its own circulation. Generally, each horseshoe vortex is made up of four vortices filaments:

- Two semi-infinite trailing vorticed (AB and CD) that begin at infinity and run parallel to the free stream and
- Thow finite bound vortices (BC and AD).

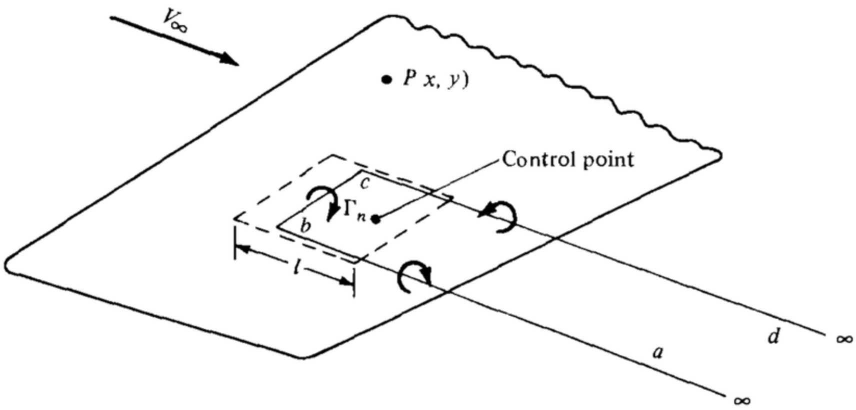

Figure 2.3 *Horseshoe vortex on a part of the wing*

Due to the indefinite distance, the effects of AD are ignored, as can be seen in Figure 2.3, so only three sections significantly influence the induced velocity. The lifting properties are represented by the bound vortex BC, while the wake is represented by the two semi-infinite vortex lines, it follows that the induced velocity, defined by the Biot-Savart law is:

$$V_p = V_{bc} + V_{b\infty} + V_{c\infty} \tag{2.9}$$

To evaluate V_p, it must be established the location of the vortex and the control point P, usually positioned respectively at ¼ and ¾ of the chord. It is also necessary to take into account the velocity induced by each horseshoe at its corresponding control point. Since the circulation is related to the Lift by the Kutta-Joukowski theorem, to obtain the total Lift we need to add up the contribution of all the panels.

2.2 Implementation in VSPAERO

VSPAERO does not strictly use the classical VLM, but instead it employs a mean surface technique, taking into account the camber effects of wings and fuselages while ignoring thickness. Wings are modeled with the same camber as the selected airfoil and are approximated by their mean surface, then divided into flat quadrilateral panels, whilst the fuselage is represented by the intersection of two mean surfaces arranged in a cross. As a ring vortex-based solver, VSPAERO distributes a finite number of ring vortices with varying intensities across the wing's surface.

During this level of analysis, viscous drag cannot be evaluated, but induced drag can be computed based on lift production.

Since VLM relies on potential flow theory, its applicability is limited to the linear aerodynamic region, within the low angle of attack flight domain and it also fails near the leading edge of the wing and the tip, where the effect of thickness is significant.

3. Geometric modelling

3.1 OpenVSP

OpenVSP is short for Open Vehicle Sketchpad. It is an open-source parametric program for aircraft geometry, originally developed by NASA. OpenVSP provides the user with the ability to create three-dimensional models of aircraft and perform engineering and aerodynamic analysis on those models. The open-source code for OpenVSP was developed by Dave Kinney at NASA Ames. The OpenVSP Web site can be accessed through the following link: http://openvsp.org.

After launch, OpenVSP displays a working window and a "Geometry Browser" (Figure 3.1) which contains a list of all the components of an airplane. Selecting a component opens its geometry window, where the user can adjust its parameters to refine the design.

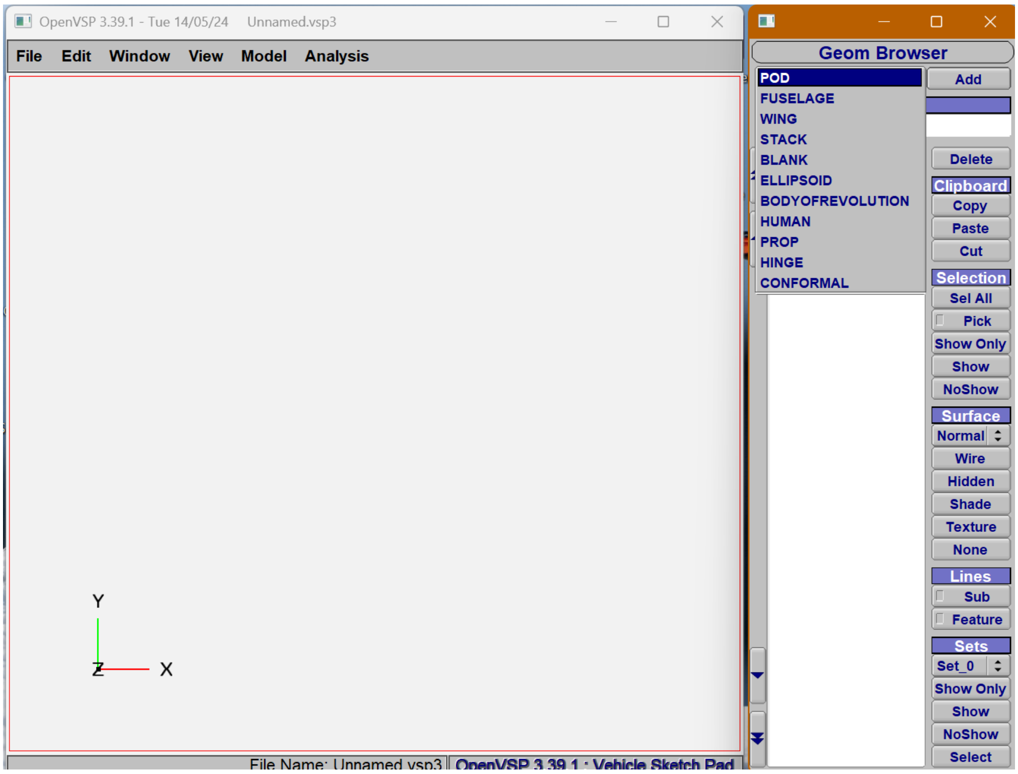

***Figure 3.1** OpenVSP initial window*

3.2 The aircraft modelling process

3.2.2 Reference Drawings

The model's dimensions were derived from manuals, photographs and reference images, such as the one in Figure 3.2.

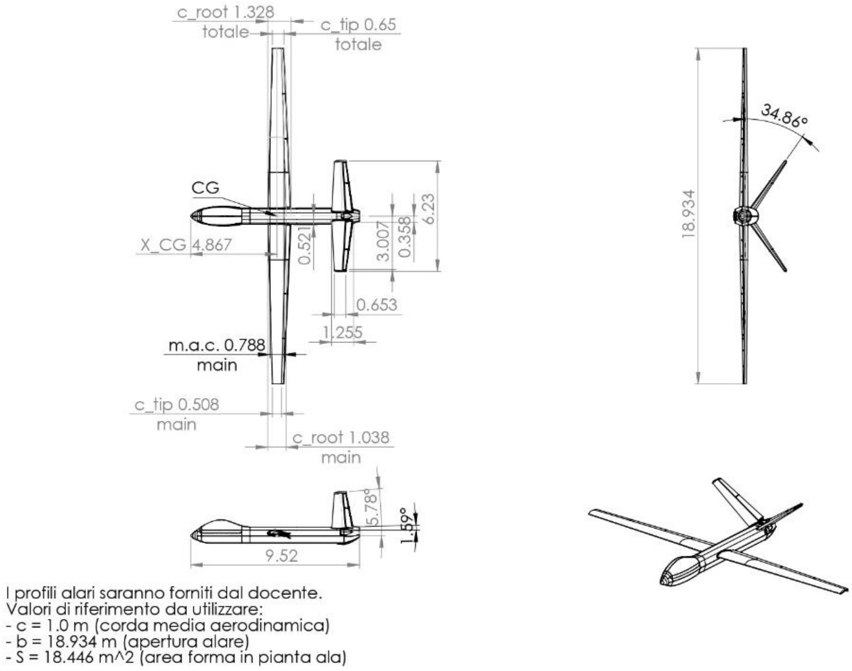

Figure 3.2 *Reference drawings*

3.2.3 Fuselage

The fuselage is the most intricate part of this UAV because of its "dome" located at the front. To model it, we start from entering the main dimensions into the Design panel and we obtain a basic shape. Later, thanks to the addition of several sections, accurately modified, the final shape, shown in Figure 3.3, has been achieved. To obtain better results when analyzed, it's also been refined the grid in chordwise and spanwise directions (U and W). The first parameter to set is the W (Figure 3.4), which controls the radial distribution of grid nodes, in the Gen panel, then we adjust the U parameter for each section (Figure 3.5 and Figure 3.6), which controls the axial grid nodes, in the XSec panel. It is best practice to set the W parameter for a fuselage from 25 to 35, depending on the curvature because, if the curvature increases, the geometry becomes intricate then it needs additional details.

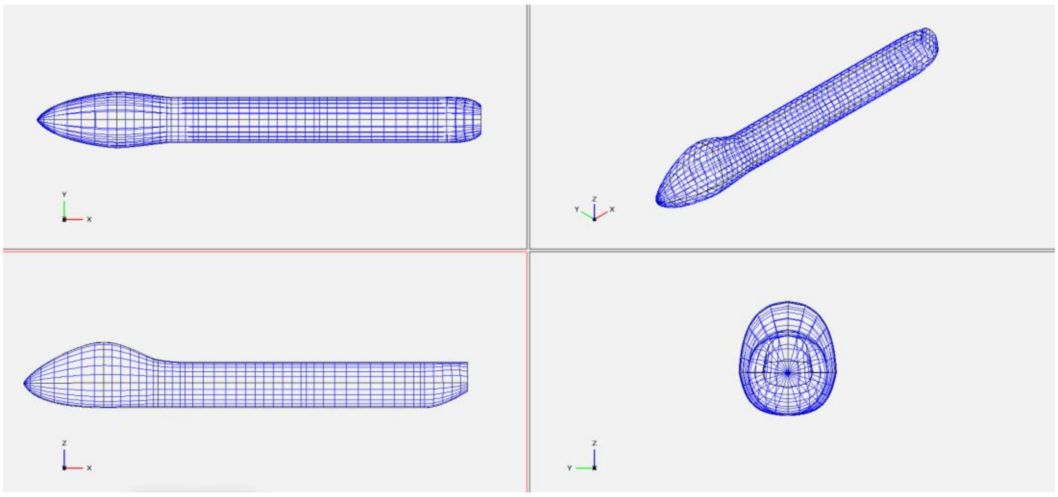

Figure 3.3 *The fuselage*

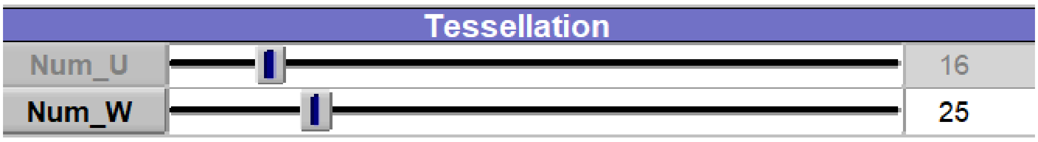

Figure 3.4 *The W parameter selector regulating the radial distribution of the panels*

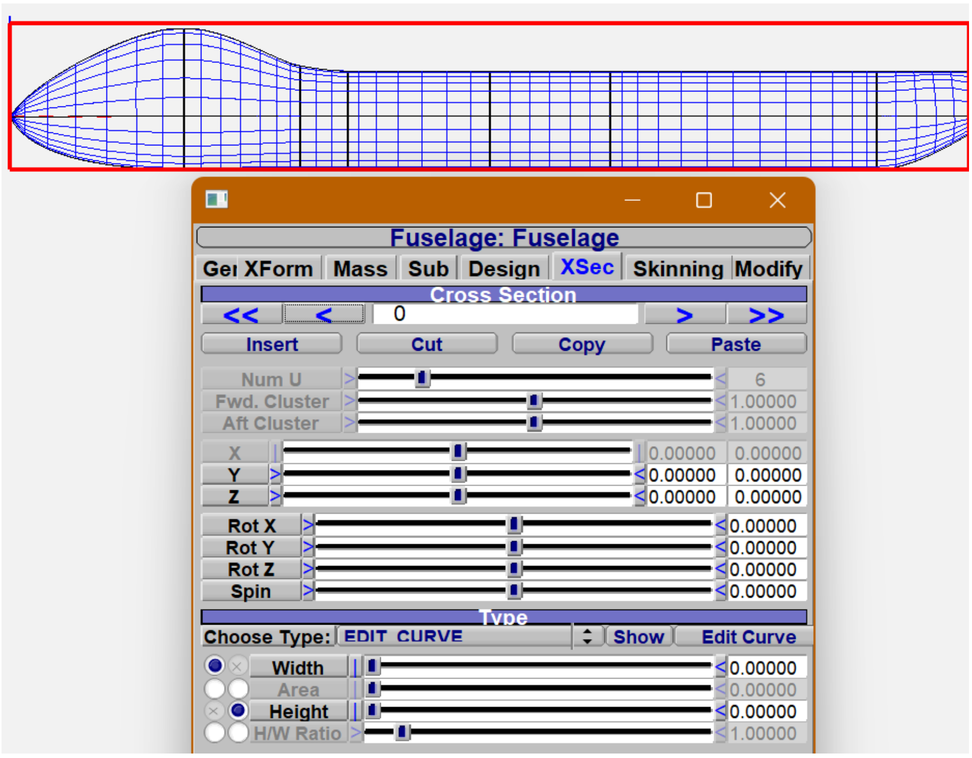

Figure 3.5 *Nose parameters*

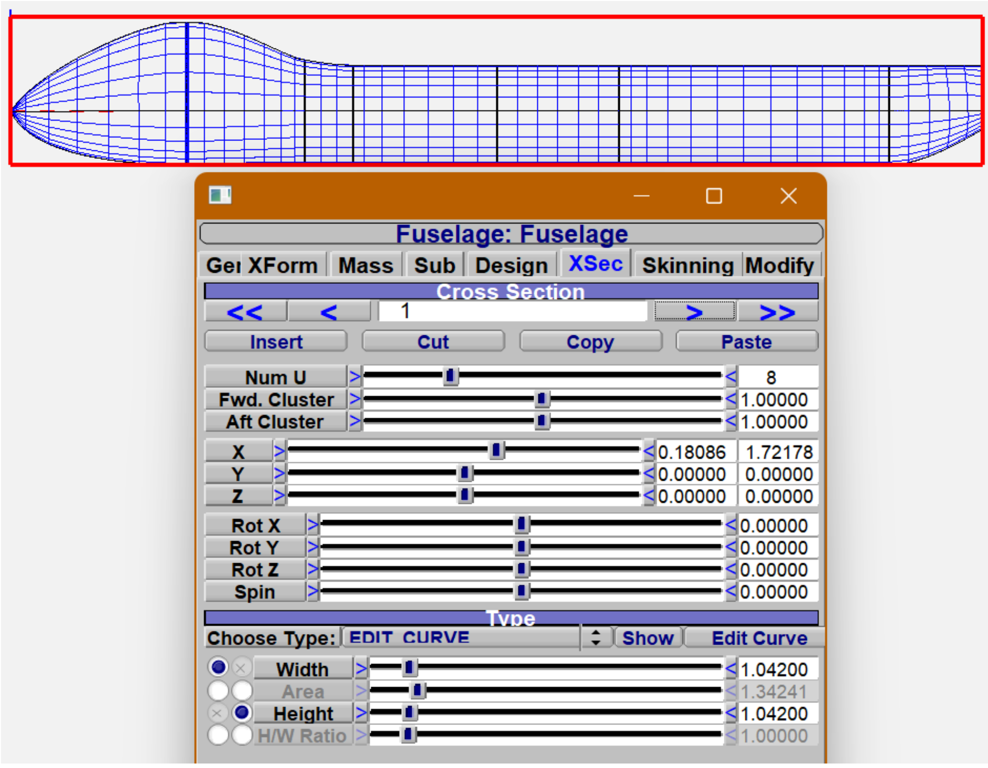

Figure 3.6 *Dome parameters*

3.2.4 Wing

To model the wing, as previously done with the fuselage, we start by setting the known parameters, obtaining an approximate shape. The exact shape is not known, but a close match is the GOE 228 (MVA H.38) represented in Figure 3.7, whose parameters have been taken from the following website: www.airfoiltools.com.

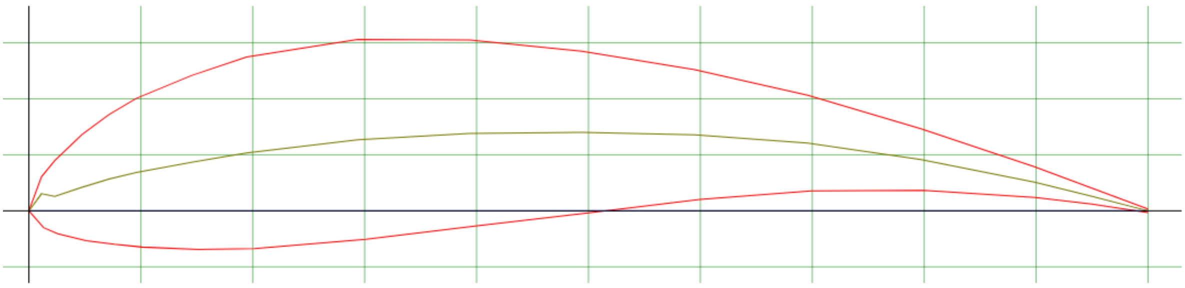

Figure 3.7 *Airfoil GOE 228*

The wing has three panels, and each one has its own twist angle, chord measurement and thickness, as reported in Table 3.1.

ID	Y (m)	t/c	twist (deg)	c (m)
1	0	0.210	0	1.328
2	0.467	0.210	0	1.295
3	2.467	0.203	0	1.155
4	9.647	0.180	-8.6	0.650

Table 3.1 *Distribution and twist law of the wing sections*

With Y=0 we refer to the midplane, consequently Y = 9.647 refers to the tip of the wing.

As with the fuselage, we also must adjust the grid for each section of the wing. For optimal result the W parameter must be set from 60 to 80. In this case, this parameter corresponds to a refinement at the leading and trailing edges of each section that allows for suitable prediction accuracy. The U parameter, adjusted from the Sect panel, has no numerical limit as the W parameter, but it must be set so the stretching ratio of the grid size, in the chordwise direction, at the mid-chord location, is 2-3. Figure 3.8 shows the final shape for the one component wing.

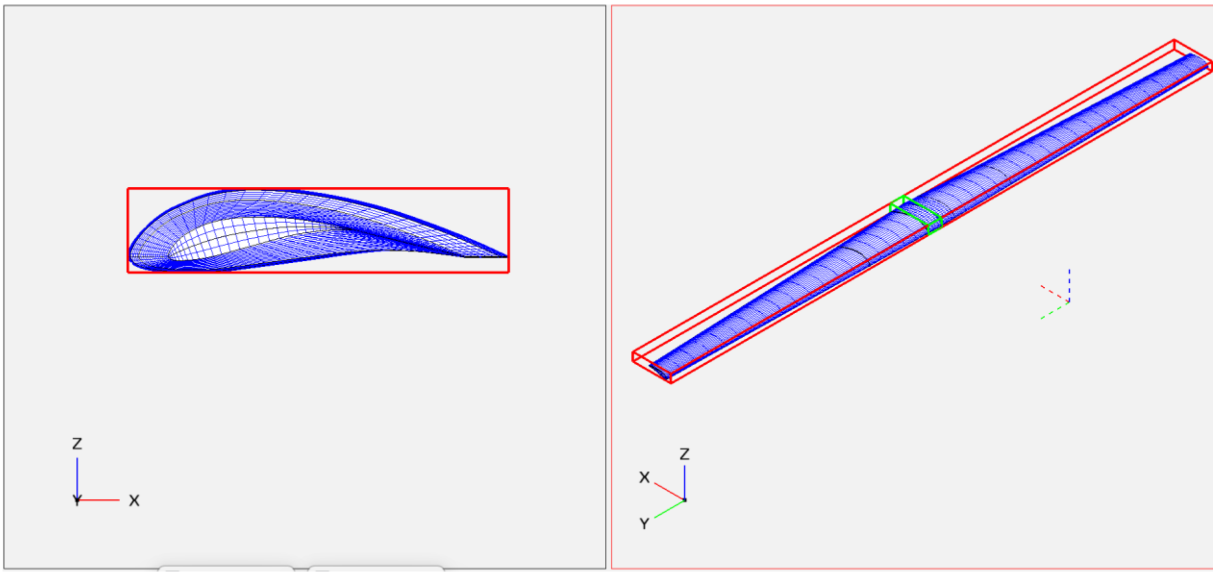

Figure 3.8 *The wing*

Two control surfaces, modelled as subsurfaces, were added to the wing trailing edge. Those are full-span flaperons with a chord ratio of 22%.

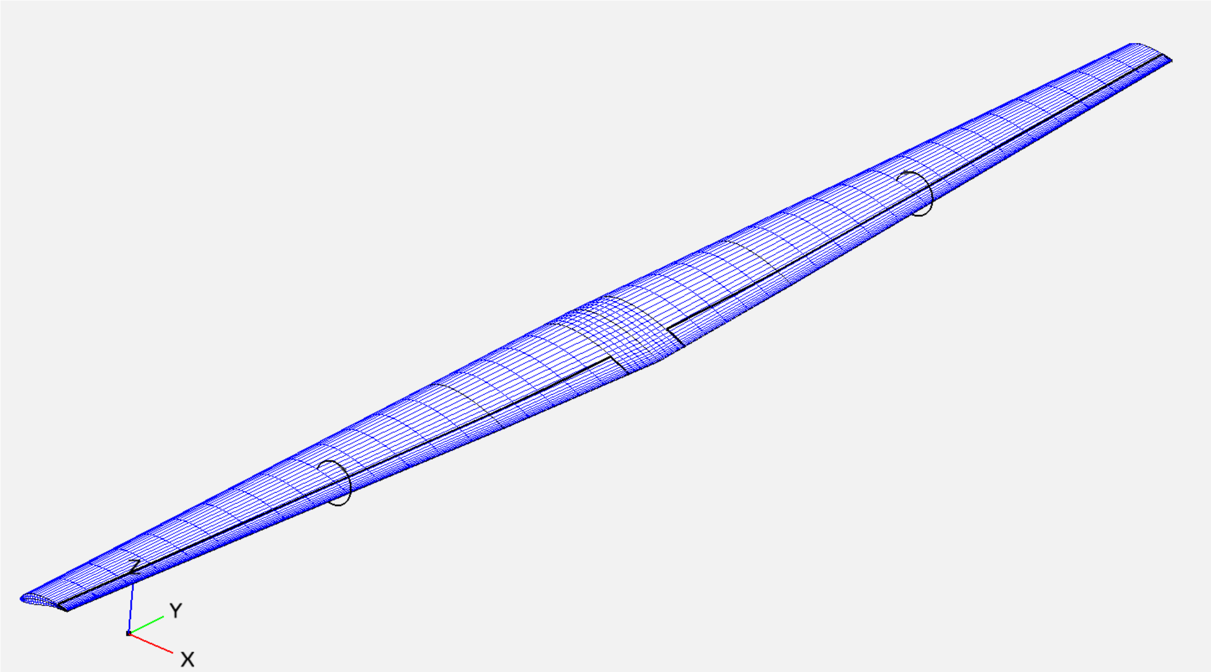

Figure 3.9 *The flaperons*

3.2.5 Tailplane

For the tailplane it’s been used a symmetrical NACA 0012 airfoil (Figure 3.10).

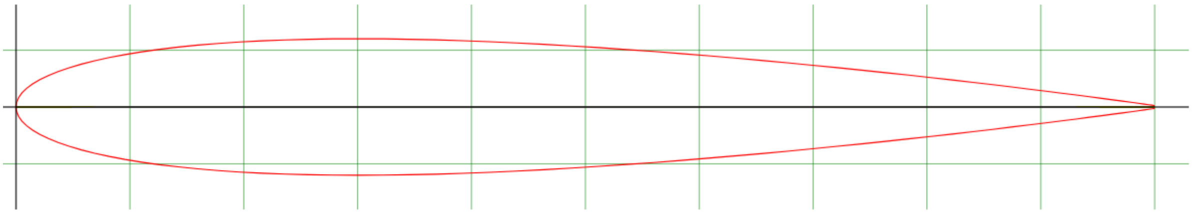

Figure 3.10 *The NACA 0012 airfoil*

To model the V-shaped tail, it was used the same process applied to the wing along with the same considerations for the grid adjustments, obtaining the design in Figure 3.11.

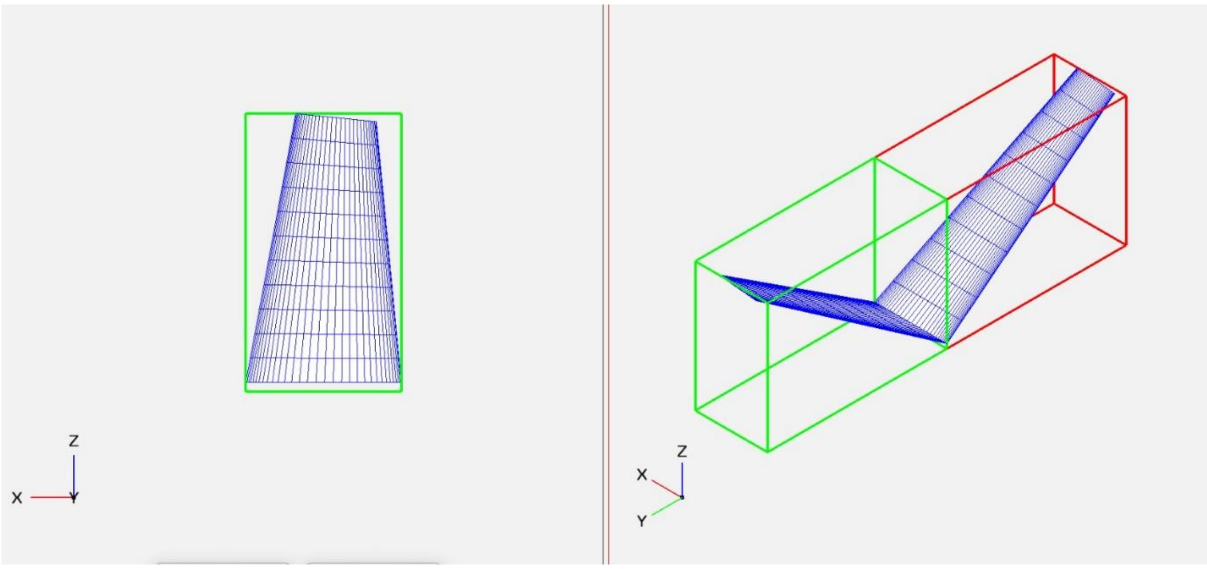

Figure 3.11 *The tailplane*

Similarly to the wing flaperons, ruddervators with a 33% chord ratio were added to the tailplane.

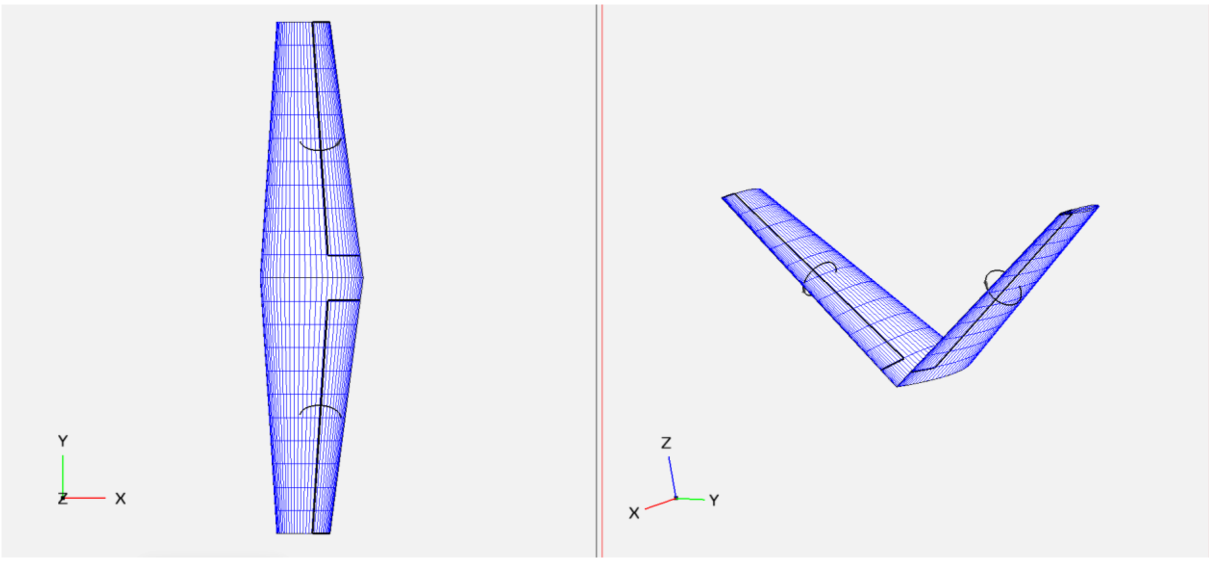

Figure 3.12 *The ruddervators*

4. Longitudinal aerodynamic analysis

To perform longitudinal aerodynamic analysis, the VSPAERO solver has been used, as previously stated. The initial settings, such as the planform area (S), the wingspan (b) and the mean aerodynamic chord (c), were determined from the aircraft model, as well as the center of gravity. The flow conditions were set to a fixed Mach number of 0 and a Reynolds number of 1E+07. The angle of attack (α) has been varied from −6° to 12° in steps of 2° and the sideslip angle (β) has been held null because of the symmetry in the X-Z plane.

4.1 Lift coefficient curves

This section focuses on the lift coefficient and how it changes at different angles of attack. Two different configurations have been considered: the complete aircraft with the one-component wing (“wing (1 comp)”) and the complete aircraft with the two-components wing (“main + flap”). The single component wing is considered with control surfaces undeflected.

It is important to point out that VSPAERO cannot simulate stall conditions, therefore only the linear portion of the lift coefficient curves is considered.

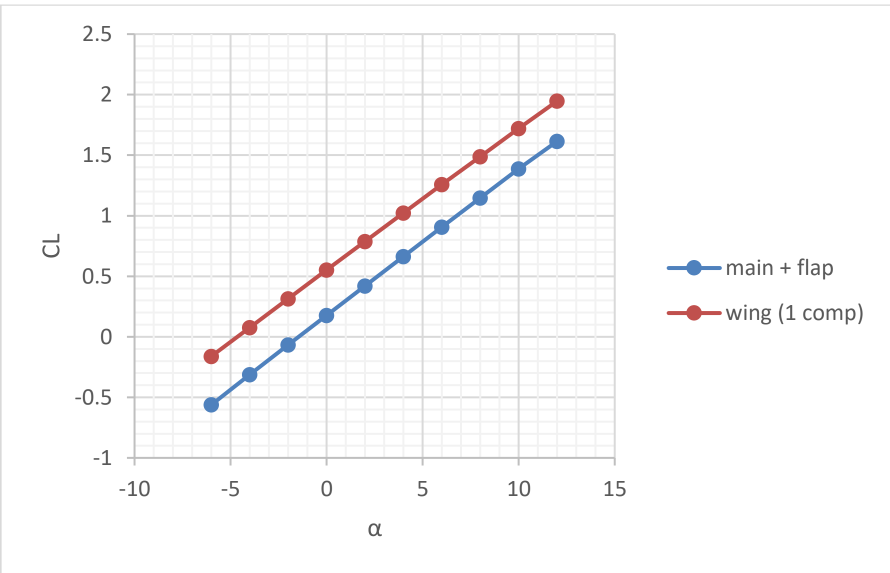

Figure 4.1 *Lift coefficients curves*

The graph in Figure 4.1 shows that the lift coefficient increases as the angle of attack increases, as to be expected, and that there is an increase in slope for the two-components wing, meaning that a unit increase in angle of attack results in a greater lift increment for the latter. We can mathematically confirm this increase in the slope of the curve by using the Excel SLOPE function, which calculates the following stability derivatives:

- Single component wing: $C_{L_\alpha} = 0.1173\ \text{deg}^{-1}$.
- Two components wing: $C_{L_\alpha} = 0.1211\ \text{deg}^{-1}$.

4.2 Pitching moment coefficient curves

This section will focus on the pitching moment coefficient with the same approach previously used for the lift. To compute the pitching moment the CG has been positioned at $\text{X} = 4.867\text{m}$.

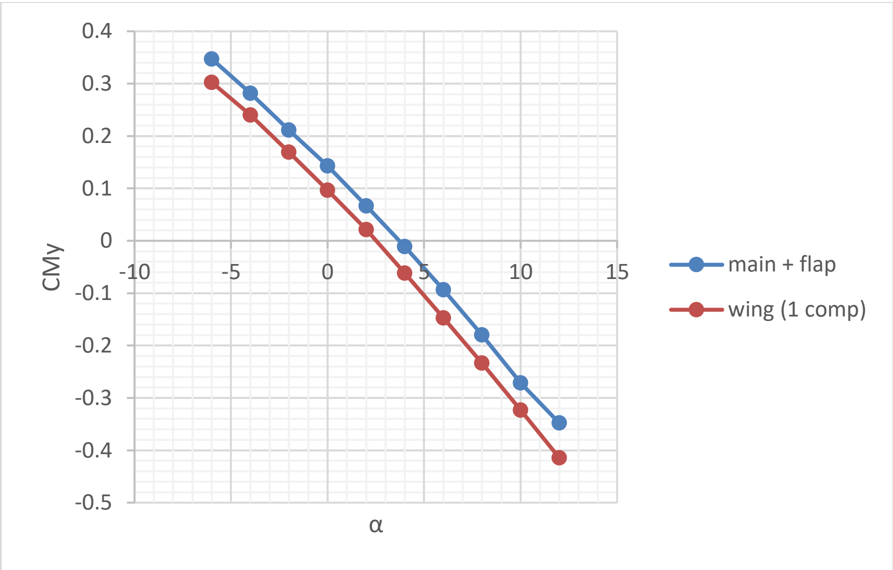

Figure 4.2 *Pitching moment coefficients curves*

The graph in Figure 4.2 shows that for both configurations exhibit longitudinal stability, since the slope of the curve is negative and the value of C_M at $\alpha = 0°$ is greater than zero. For the two-component wing there is a slight reduction in the absolute value of the slope of the curve, as confirmed by the calculation of the C_{M_α} which is the pitching moment curve slope, obtained with the Excel SLOPE function:

- Single component wing: $C_{M_\alpha} = -0.0401\ \text{deg}^{-1}$.
- Two components wing: $C_{M_\alpha} = -0.0390\ \text{deg}^{-1}$.

The values of C_{L_α} and C_{M_α} allow for the calculation of the Neutral Point (NP) for both configurations:

$$\frac{x_N}{c} = \frac{x_{CG}}{c} - \frac{C_{M_\alpha}}{C_{L_\alpha}} \tag{4.1}$$

The following results are in fractions of the mean aerodynamic chord (c) with the CG at 25%:

- Single component wing: $\frac{x_N}{c} = 0.592$
- Two components wing: $\frac{x_N}{c} = 0.572$.

4.3 Polar and Aerodynamic efficiency curves

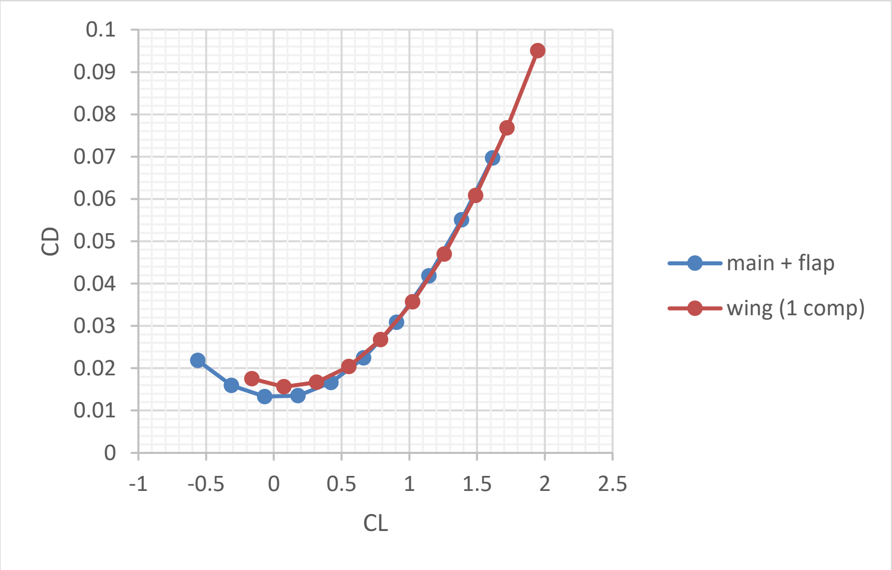

Figure 4.3 *Polar curves*

Figure 4.3 shows a slight reduction in drag with the addition of the flap, mainly because the configuration with the flap generates less lift, therefore it has less induced drag.

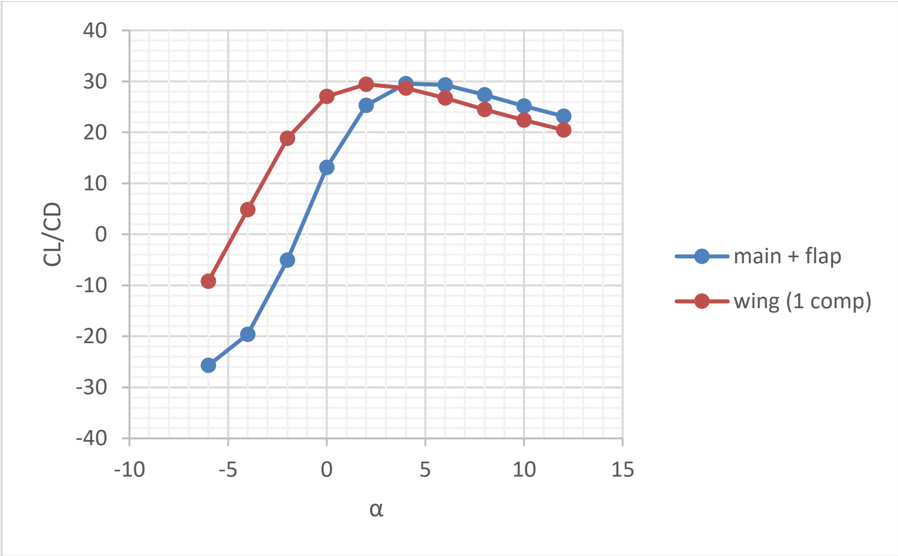

Figure 4.4 *Aerodynamic efficiency curves*

In Figure 4.4, we can observe a higher lift-to-drag ratio (C_L/C_D), indicating a greater efficiency for the one component wing at lower values of angle of attack. However, the advantage of using a flap becomes evident as the angle of attack increases.

4.4 Impact of control surfaces on longitudinal aerodynamics

The second phase of this analysis focuses on the effects of the deflections of the flaperons on the wing and the ruddervators on the tail. These simulations were performed on the single component wing only. The analysis has been conducted applying the following deflections:

- Flaperons: 0°, 11.25°, 26.25°
- Ruddervators: 0°, -10°, -20°.

4.4.1 Lift

First, the analyses were performed by symmetrically rotating the flaperons with neutral ruddervators (deflection at 0°), obtaining the results in the following charts.

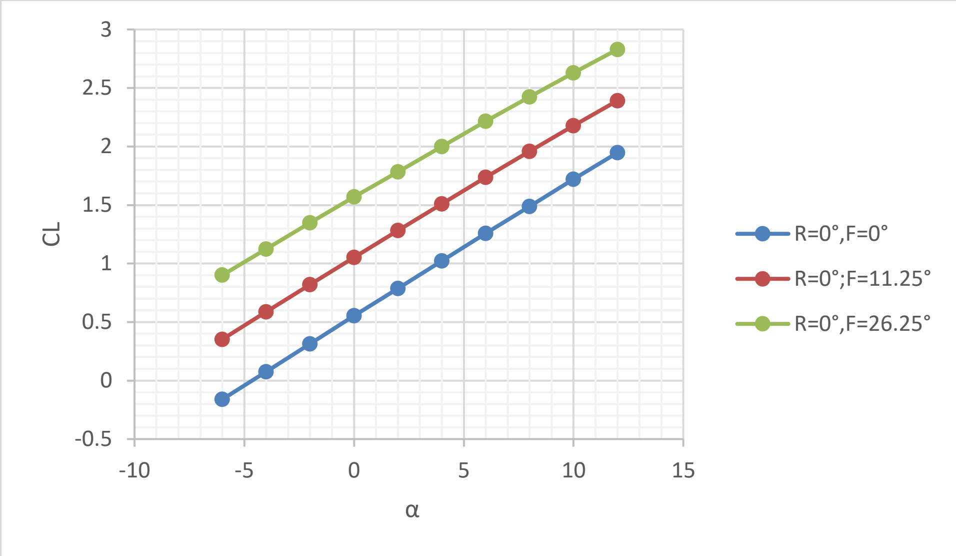

***Figure 4.5 C_L** at a fixed ruddervators deflection*

For a fixed ruddervators deflection, the lift coefficients increase as the flaperons deflections increases, as clearly shown in Figure 4.5. This demonstrates the flaperons' effectiveness in increasing lift.

Figure 4.6 shows the effect of varying ruddervators deflection with a fixed flaperons deflection. We observe that an increase in negative ruddervators' deflection, results in a decrease in C_L.

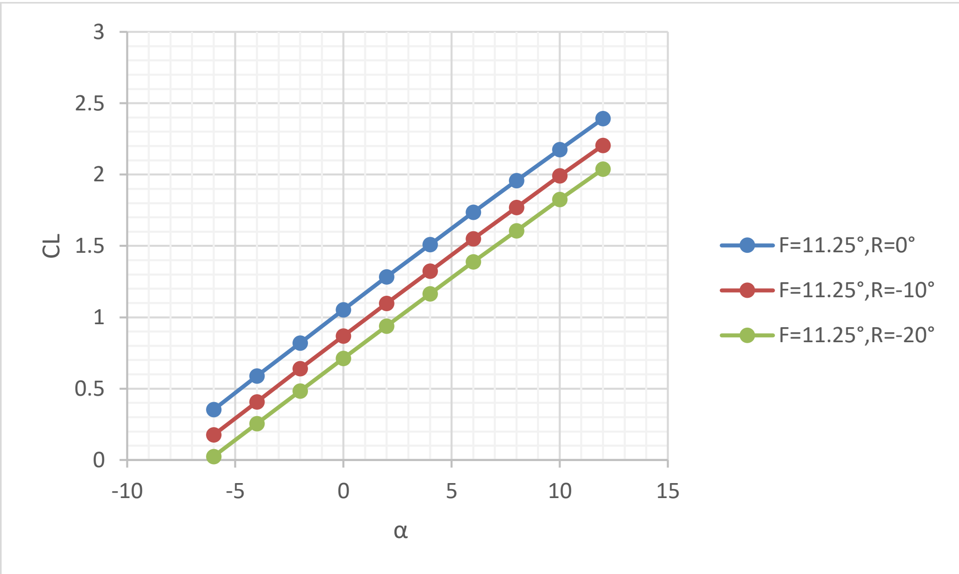

***Figure 4.6 C_L** at a fixed flaperons deflection*

The same behaviors have been observed fixing the flaperons deflection at 0° and 26.25°. The charts are not reported here for the sake of brevity.

4.4.2 Pitching moment

Using the same approach, the variation of the pitching moment coefficient with the control surfaces' deflection has been analyzed (Figure 4.7 and 4.8).

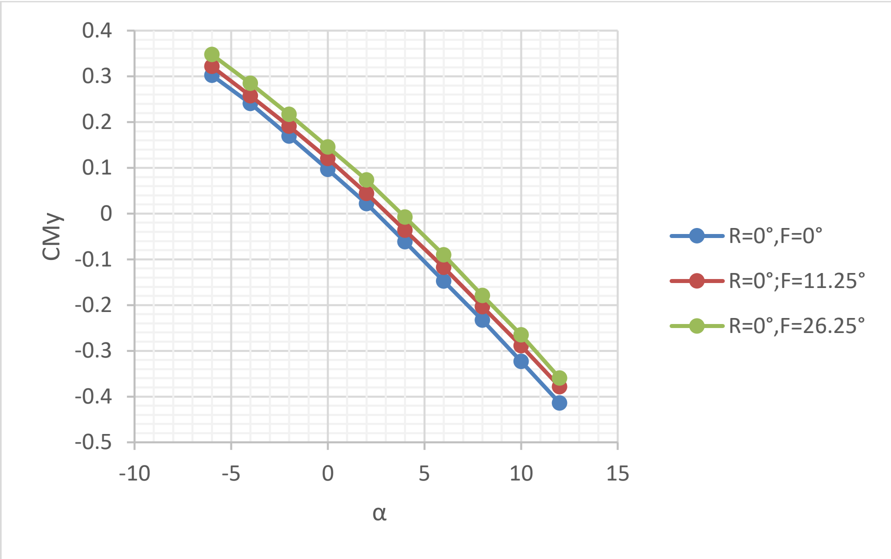

Figure 4.7 C_M *at a fixed ruddervators deflection*

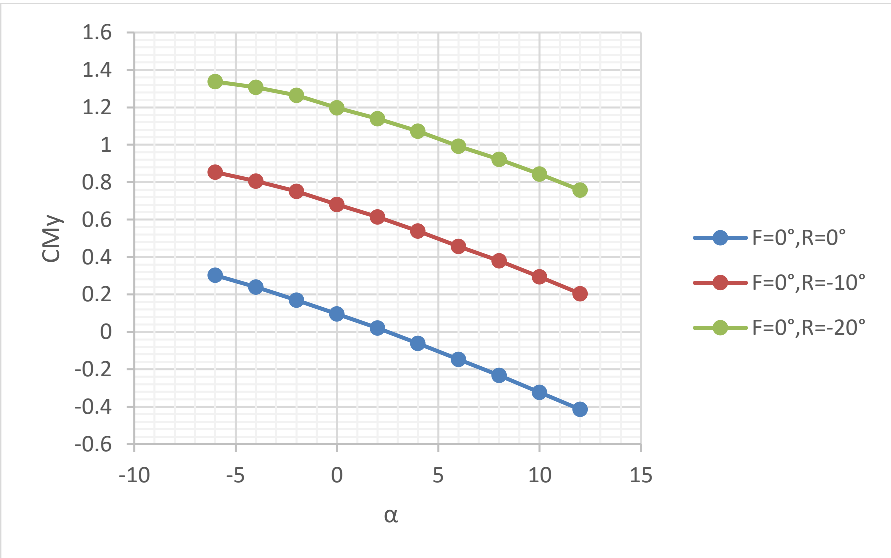

Figure 4.8 C_M *at a fixed flaperons deflection*

Similar results for the same curves by fixing the flaperons at 11.25° and 26.25°.

Using the following formula, the control derivatives in Table 4.1 have been estimated:

$$C_{M_\delta} = \frac{C_{M_0}(\delta) - C_{M_0}(\delta = 0°)}{\delta} \tag{4.2}$$

$\boldsymbol{\delta f}$ (deg)	$\boldsymbol{\delta r}$ (deg)	$\boldsymbol{C_{M_{\delta f}}}$	$\boldsymbol{C_{M_{\delta r}}}$
0	-10	n.a.	-0.0585
0	-20	n.a.	-0.0551
11.25	0	0.0021	n.a.
11.25	-10	0.0020	-0.0607
11.25	-20	0.0019	-0.0561
26.25	0	0.0019	n.a.
26.25	-10	0.0018	-0.0631
26.25	-20	0.0017	-0.0573

Table 4.1 *Control derivatives*

4.4.3 Polar curves

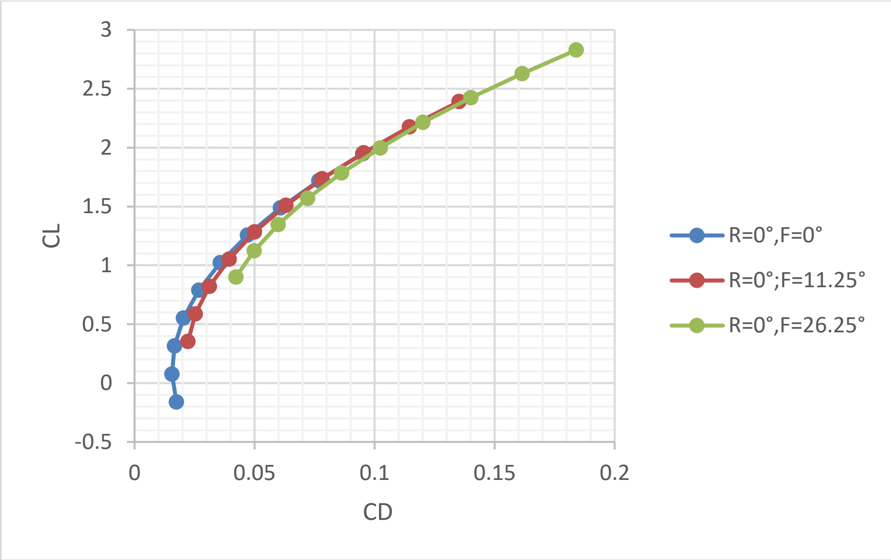

Figure 4.9 *Polar curves at fixed ruddervators deflection*

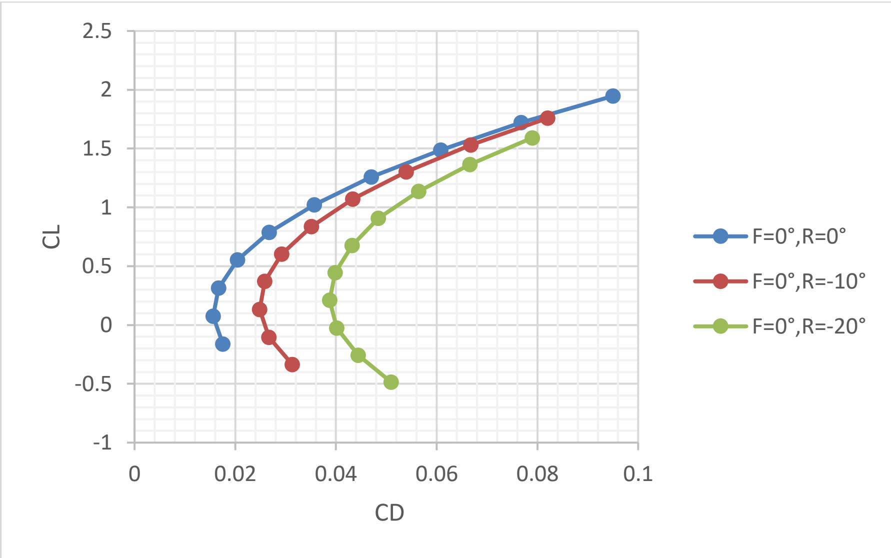

Figure 4.10 *Polar curves at* $\boldsymbol{\delta f}$ *=0°*

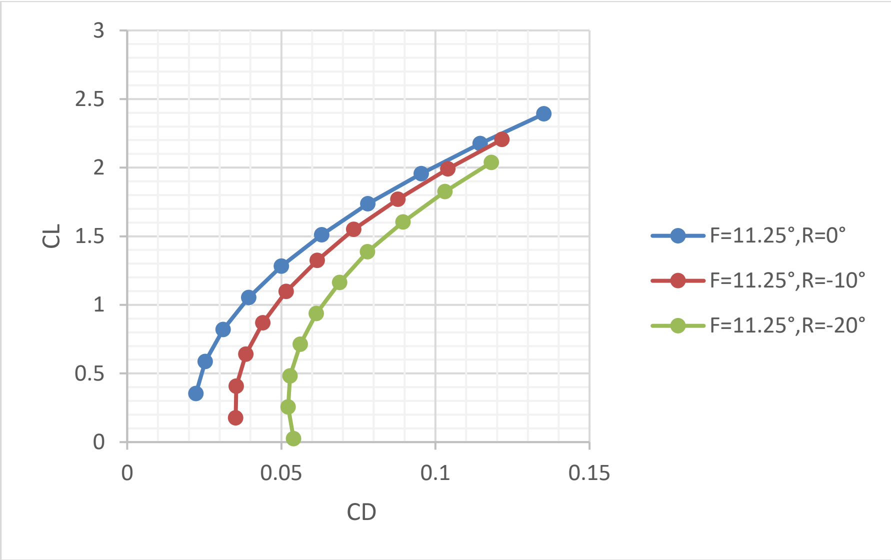

Figure 4.11 *Polar curves at δf =11.25°*

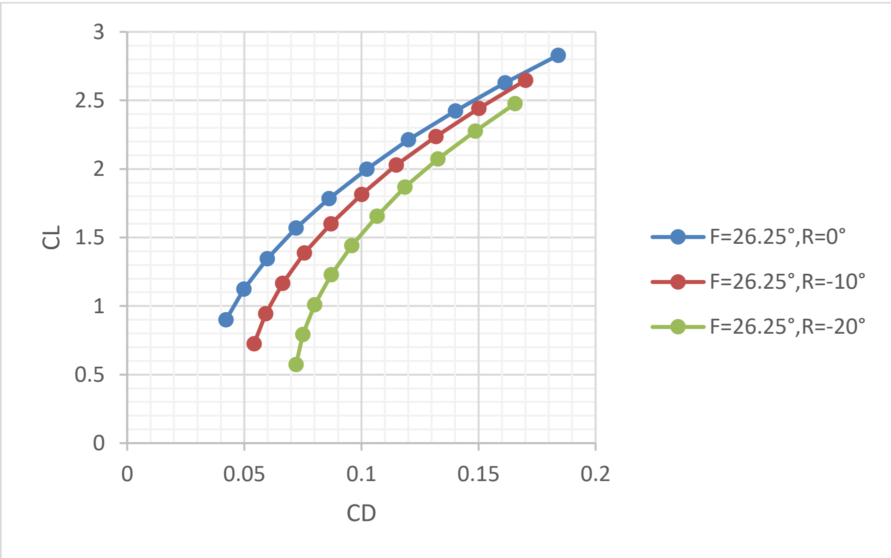

Figure 4.12 *Polar curves at δf =26.25°*

Figure 4.9 shows that for a fixed ruddervators deflection, there is a general increase in lift as the flaperons deflection increase, accompanied by a rise in aerodynamic drag. The same behavior has been observed when the flaperons deflection were fixed and the ruddervators were moved. The deflection of the ruddervators, as shown in Figure 4.10 to 4.13, caused a reduction in lift and an increment in drag, as the angle of deflection increased.

To end this analysis, Figures 4.13 and 4.14 below illustrate the wake patterns at various angles of attack, specifically at 0°, 4°, and 8°, comparing the behavior of the one component wing and two components wing.

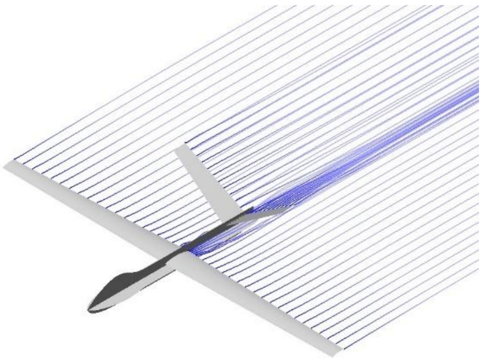

Figure 4.13 *Trailing wake at* $\boldsymbol{\alpha = 0}$°*and* $\boldsymbol{\alpha = 8}$° *for the single component wing*

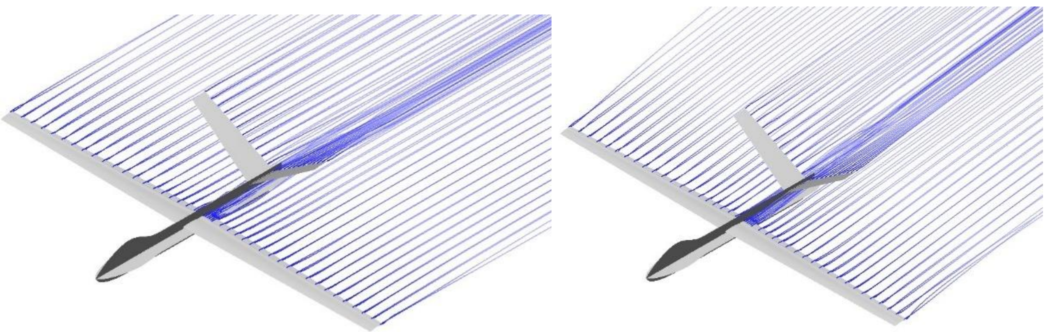

Figure 4.14 *Trailing wake at α=0°and α=8° for the two components wing*

5. Lateral-Directional aerodynamic analysis

The conditions for conducting this analysis are similar to those applied in the longitudinal analysis. The Mach and Reynolds numbers are kept constant. However, in this case, the angle of attack α is fixed at 0°, while the sideslip angle β is varied from −4° to 16° in steps of 2°, with the X-Z symmetry disabled. The coefficients discussed in this analysis are pitching moment coefficient C_{My}, rolling moment coefficient C_{Ml}, yawing moment coefficient C_{Mn}, and side force coefficient C_{Fy}, as well as the lift and drag coefficient (C_L and C_D). As previously done in Chapter 4, the analysis has been performed first on the single component wing and then on the two-components wing.

5.1 Lateral-directional stability

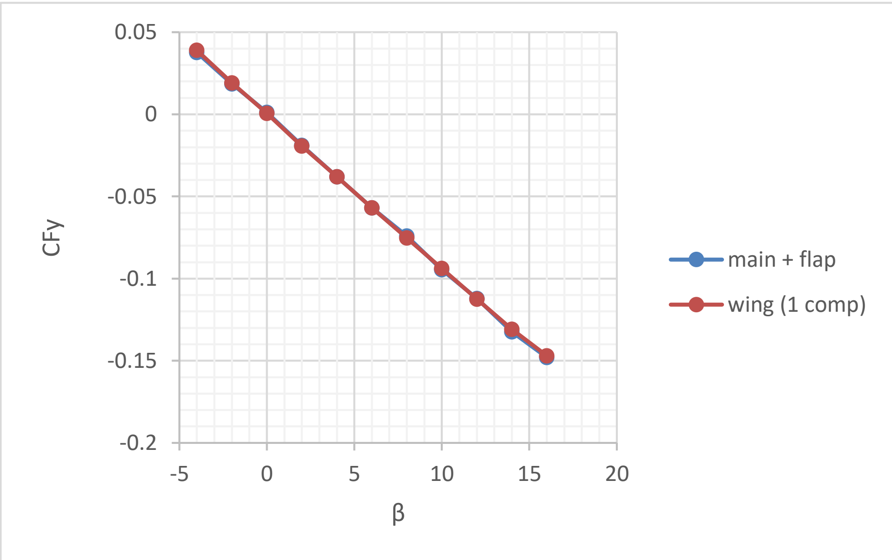

Figure 5.1 *Side force coefficient curves*

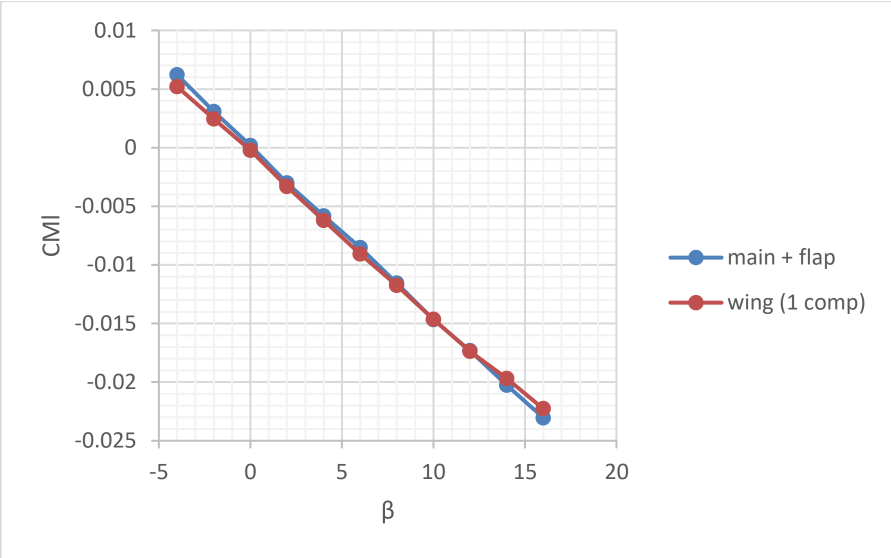

Figure 5.2 *Rolling moment coefficient curves*

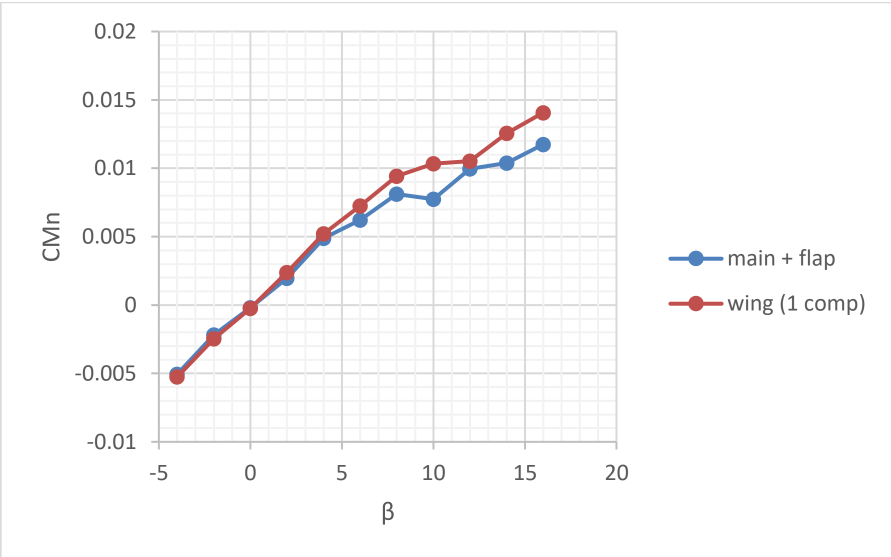

Figure 5.3 *Yawing moment coefficient curves*

The graphs in Figure 5.1, Figure 5.2 and Figure 5.3 show that, because of the airplane symmetry, all the coefficients are nearly zero at $\beta = 0°$. The negative slope in Figure 5.1 and the positive slope in Figure 5.3 are the demonstration that the UAV exhibits both lateral and directional stability. It's important to note that the coefficients C_{Fy}, C_{Ml} and C_{Mn} are presented in the body reference frame (BRF) with origin at the center of gravity (CG), which is the assigned reference point.

Using the Excel SLOPE function, the following stability derivatives have been estimated:

- $C_{Fy_\beta} = -0.0093 \text{ deg}^{-1}$.

- $C_{Ml_\beta} = -0.0014\ \text{deg}^{-1}$.
- $C_{Mn_\beta} = 0.0009\ \text{deg}^{-1}$.

5.2 Impact of sideslip angle on aerodynamic coefficients

To complete the analysis of lateral-directional stability, it is essential to examine the cross-effects of the sideslip angle (β) on the aerodynamic coefficients. In particular, we have analyzed how the sideslip angle influences the lift (C_L) in Figure 5.4, drag (C_D) in Figure 5.5, and pitching moment coefficient (C_{My}) in Figure 5.6, providing further information on the wing's response to lateral perturbations.

It can be observed that, although with different values, the lift coefficient trend with the sideslip angle is quite flat. The drag coefficient exhibits a larger variation, attributed to the different incidence of the two halves of the V-tail layout. The pitching moment coefficient shows a significant and unrealistic variation with the sideslip angle. This has been attributed to the aerodynamic interference calculated by VSPAERO.

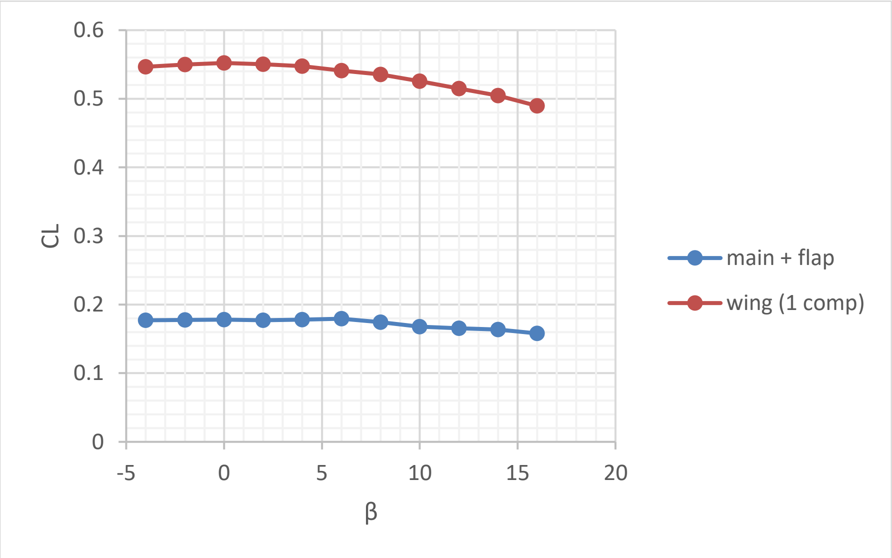

Figure 5.4 *C_L vs β*

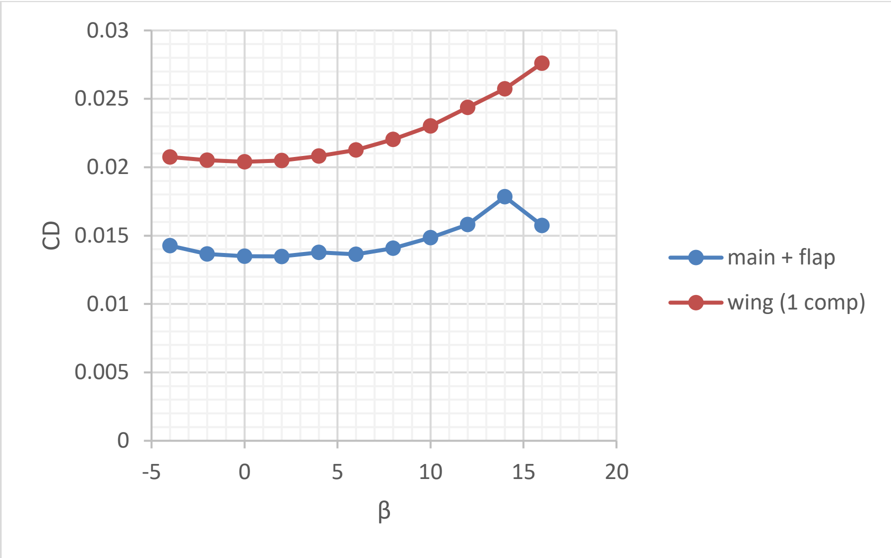

Figure 5.5 *C_D vs* $\boldsymbol{\beta}$

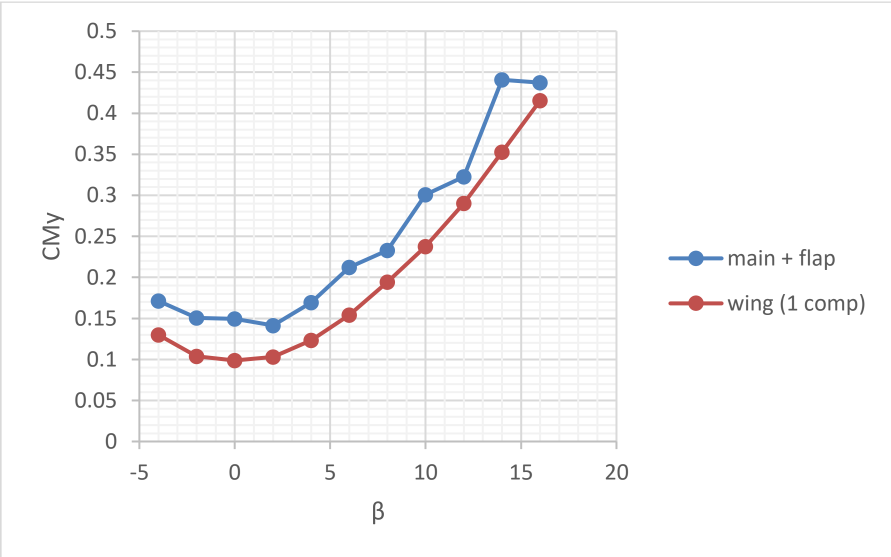

Figure 5.6 *C_{My} vs β*

6. Conclusions

This thesis has shown how the combination of OpenVSP and VSPAERO offers a valuable and efficient approach for preliminary aerodynamic analysis in aircraft design, providing rapid insights into aerodynamic behavior without the need for extensive Computational Fluid Dynamics (CFD) simulations and significantly accelerating the early stages of the design process. However, it is important to acknowledge the inherent limitations of this method. In particular, VSPAERO, is based on simplifications that affect the reliability of results, especially regarding the interactions between control surfaces and the accurate representation of the aircraft's dynamics. The main limitations include:

- Single component wing vs wing with flap: VSPAERO does not fully capture the effect of movable surfaces, as it ignores viscous effects and flow separation.
- Cross-effects between control surfaces: the interaction between flaperon and ruddervators is only partially accounted for, as VLM assumes potential flow and neglects nonlinear phenomena.
- Drag prediction limitations: induced drag is estimated, but parasitic drag and three-dimensional flow effect of the fuselage and tail are not considered.

Bibliography

[1] Advanced UAV aerodynamics, Flight stability and control, Pascual Marqués, Andrea Da Ronch John Wiley & Sons, Apr 27, 2017.

[2] Software Testing: VSPAERO, Floris Mariën, Prof. Dr.-Ing. Dieter Scholtz, 16/07/2021.

[3] OpenVSP website: http://openvsp.org

[4] Airfoil Tools website: http://airfoiltools.com

[5] OpenVSP ground school website: https://vspu.larc.nasa.gov

[6] Avions Legendaires, Elbit Hermes 900.